

This article appeared in a journal published by Elsevier. The attached copy is furnished to the author for internal non-commercial research and education use, including for instruction at the authors institution and sharing with colleagues.

Other uses, including reproduction and distribution, or selling or licensing copies, or posting to personal, institutional or third party websites are prohibited.

In most cases authors are permitted to post their version of the article (e.g. in Word or Tex form) to their personal website or institutional repository. Authors requiring further information regarding Elsevier's archiving and manuscript policies are encouraged to visit:

<http://www.elsevier.com/copyright>



## Periodic occurrence of chaotic behavior of homoclinic tangles

Q.D. Wang<sup>\*</sup>, A. Oksasoglu<sup>1</sup>

Department of Mathematics, University of Arizona, Tucson, AZ 85721, United States

### ARTICLE INFO

#### Article history:

Received 4 May 2009

Accepted 14 December 2009

Available online 21 December 2009

Communicated by B. Sandstede

#### Keywords:

Chaos

Dissipative saddle

### ABSTRACT

In this article, we illustrate, through numerical simulations, some important aspects of the dynamics of the periodically perturbed homoclinic solutions for a dissipative saddle. More explicitly, we demonstrate that, when homoclinic tangles are created, three different dynamical phenomena, namely, horseshoes, periodic sinks, and attractors with Sinai–Ruelle–Bowen measures, manifest themselves *periodically* with respect to the magnitude of the forcing function. In addition, when the stable and the unstable manifolds are pulled apart so as not to intersect, first, rank 1 attractors, then quasi-periodic attractors are added to the dynamical scene.

© 2009 Elsevier B.V. All rights reserved.

### 1. Introduction

As complicated dynamical objects, periodically perturbed homoclinic solutions have been studied extensively in history. They are among the few that have occupied the center stage of chaos theory since the time of Henry Poincaré [1–4]. Literature studies on rigorous mathematical analysis and on numerical simulations are numerous and it is too vast a subject to be systematically reviewed here. For previous results and the related history we refer the reader to [5–9] and the references therein.

In this paper, we illustrate, through numerical simulations, some of the important findings of a recent dynamics theory [10,11]. This theory is applicable to a class of second-order systems with homoclinic solutions to a dissipative saddle point. The conclusions from [10,11] that are to be verified are as follows:

**(I) (Dynamical objects)** When homoclinic tangles are created by time-periodic perturbations, there are three main dynamical scenarios competing in the space of forcing parameters:

- (the *transient tangle*) there exist open sets of parameters such that the entire homoclinic tangle is a uniformly hyperbolic horseshoe of infinitely many symbols;
- (the *non-chaotic tangle*) there exist open sets of parameters such that the homoclinic tangle admits periodic sinks; and
- (the *chaotic tangle*) there exist positive measure sets of parameters such that the homoclinic tangle admits Sinai–Ruelle–Bowen (SRB) measure [12–14].

**(II) (Multiplicative periodicity)** Let  $T$  be the period of the forcing function in time,  $\beta$  be the positive eigenvalue of the perturbed saddle, and  $\mu$  be the magnitude of the forcing. The theory of [11] claims that there is a well-defined pattern for the occurrences of the three dynamical scenarios of **(I)**; and this pattern materializes over every  $\mu$ -interval  $(\mu_1, \mu_2)$  satisfying  $\mu_2/\mu_1 \approx e^{\beta T}$ , repeating infinitely many times as  $\mu \rightarrow 0$ .

**(III) (Rank 1 attractors)** When the stable and the unstable manifolds of the perturbed saddle are pulled apart, the dynamical behavior manifests itself in three different forms, again competing in the parameter space:

- (the *non-chaotic attractor*) there are open sets of parameters such that the attractors admit periodic sinks, and
- (the *rank 1 attractor*) there are positive measure sets of parameters such that the attractors are rank 1 attractors [15–17] with SRB measure, and fully stochastic behavior;
- (*Hénon-like attractors*) there are also Hénon-like attractors [18] associated with transversal homoclinic tangency of the stable and unstable manifolds of the periodic saddle.

**(IV) (Quasi-periodic attractors)** If the stable and the unstable manifolds of the perturbed saddle are pulled further apart, then there exist attractive tori in the extended phase space made of solutions of two frequencies. Of those two frequencies, one is the frequency of the forcing function, and the other depends sensitively on  $\mu$  and other parameters.

**(I)(a)–(c)** and **(IV)** have been previously encountered in a sporadic fashion in numerical simulations. **(II)** and **(III)**, on the other hand, are completely new. For precise definitions of various dynamical terms used in the statements above, we refer the reader to a recent tutorial paper [19].

Physical measures [20] are dynamical objects that dictate the asymptotic statistics of a collection of positive Lebesgue measure

<sup>\*</sup> Corresponding author. Tel.: +1 520 360 6641.

E-mail addresses: [dwang@math.arizona.edu](mailto:dwang@math.arizona.edu) (Q.D. Wang), [alioksas@email.arizona.edu](mailto:alioksas@email.arizona.edu) (A. Oksasoglu).

<sup>1</sup> Also with Honeywell, Inc.

**Table 1**  
Parameter values used in simulations.

$(q_0, p_0) = (0.01, 0.0)$		
$\lambda_0$	0.5	1.0
$\gamma_0$	0.577028548901	1.122987493358
$T$	1	2

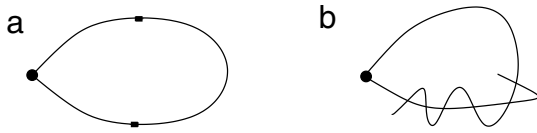


**Fig. 1.** Homoclinic solutions. (a) Unperturbed homoclinic solution. (b) Homoclinic tangle.

sets of orbits in phase space. Attractive quasi-periodic tori and periodic sinks induce physical measures representing stable dynamics. SRB measures, on the other hand, are physical measures representing chaotic dynamics. Saddles and horseshoes, generally speaking, do not support physical measures because the collection of orbits that they attract has zero Lebesgue measure. It is important to note that, of the dynamical behaviors stated in **(I)** above, only **(I)(b)** and **(I)(c)** represent physical measures.

In this article, we adopt the probabilistic point of view that, if numerical integrations of a solution starting from a given initial condition result in an asymptotically stable distribution, it will likely lead us to a physical measure. We also adopt a similar probabilistic point of view that, when a parameter is involved, the kinds of physical measures observed will likely be supported by a parameter set of positive Lebesgue measure.

**2. System under study**

We start with an autonomous ordinary differential equation defined on the plane:

$$\frac{d^2q}{dt^2} - q + q^2 = 0. \tag{1}$$

Defining  $p = dq/dt$ , we assume that Eq. (1) has a saddle fixed point  $X^* = (q, p) = (0, 0)$  and a solution  $\ell(t) = (a(t), b(t))$  such that  $\lim_{t \rightarrow \pm\infty} \ell(t) = X^*$ .  $\ell(t)$  is a homoclinic solution to  $X^*$  (see Fig. 1(a)).

Next, we add a nonlinear damping term to Eq. (1) to form a new autonomous equation

$$\frac{d^2q}{dt^2} + (\lambda - \gamma q^2) \frac{dq}{dt} - q + q^2 = 0, \tag{2}$$

where  $\lambda, \gamma > 0$  are parameters.  $(q, p) = (0, 0)$  is now a dissipative saddle. Let  $\lambda = \lambda_0 > 0$ . Then, for  $\lambda_0$  sufficiently small there exists a  $\gamma = \gamma_0 > 0$  uniquely determined by  $\lambda_0$  such that Eq. (2) has a homoclinic solution as depicted in Fig. 1(a). Although  $\lambda$  small was assumed for a rigorous proof [11], it is readily verified by numerical simulations that homoclinic solutions exist for much larger values of  $\lambda$ .

Then, we add a time-periodic forcing to Eq. (2) to obtain

$$\frac{d^2q}{dt^2} + (\lambda - \gamma q^2) \frac{dq}{dt} - q + q^2 = \mu \sin \omega t, \tag{3}$$

where  $\mu$  is a parameter representing the magnitude of the forcing, and  $\omega$  is the forcing frequency. It is well-known that the addition of such a time-periodic forcing in Eq. (3) leads to homoclinic tangles and chaotic dynamics (see Fig. 1(b)). What we intend to illustrate here is that the dynamical objects of **I(a)**–(c) repeat themselves periodically with respect to the forcing magnitude  $\mu$ .

**Table 2**  
Multiplicative periodicity on  $\mu$ .

$\lambda = 0.5$			
$\gamma = 0.577028548901$			
$T = 1.0$			
$\beta = 0.78077641$			
Theoretical multiplicity = $e^{\beta T} = 2.1831$			
$\mu$	Dynamical behavior	Actual ratio	Frequency of occurrence (%)
$1.577 \cdot 10^{-3}$	Transient tangle (I)(a)	–	94.23
$7.774 \cdot 10^{-4}$	Chaotic tangle (I)(c)	–	1.61
$7.637 \cdot 10^{-4}$	Non-chaotic tangle (I)(b)	–	4.16
$7.284 \cdot 10^{-4}$	Transient tangle (I)(a)	2.1650	94.28
$3.574 \cdot 10^{-4}$	Chaotic tangle (I)(c)	2.1752	3.18
$3.449 \cdot 10^{-4}$	Non-chaotic tangle (I)(b)	2.2143	2.54
$3.349 \cdot 10^{-4}$	Transient tangle (I)(a)	2.1750	94.54
$1.635 \cdot 10^{-4}$	Chaotic tangle (I)(c)	2.1859	1.49
$1.608 \cdot 10^{-4}$	Non-chaotic tangle (I)(b)	2.2143	3.97
$1.536 \cdot 10^{-4}$	Transient tangle (I)(a)	2.1803	94.42
$7.505 \cdot 10^{-5}$	Chaotic tangle (I)(c)	2.1785	2.37
$7.308 \cdot 10^{-5}$	Non-chaotic tangle (I)(b)	2.2003	3.21
$7.041 \cdot 10^{-5}$	Transient tangle (I)(a)	2.1815	95.00
$3.415 \cdot 10^{-5}$	Chaotic tangle (I)(c)	2.1977	1.91
$3.342 \cdot 10^{-5}$	Non-chaotic tangle (I)(b)	2.1867	3.09
$3.224 \cdot 10^{-5}$	Transient tangle (I)(a)	2.1839	94.29
$1.574 \cdot 10^{-5}$	Chaotic tangle (I)(c)	2.1696	3.17
$1.504 \cdot 10^{-5}$	Non-chaotic tangle (I)(b)	2.2221	2.54
$1.474 \cdot 10^{-5}$	Transient tangle (I)(a)	2.1872	94.53
$7.190 \cdot 10^{-6}$	Chaotic tangle (I)(c)	2.1892	4.00
$6.931 \cdot 10^{-6}$	Non-chaotic tangle (I)(b)	2.1700	1.71
$6.732 \cdot 10^{-6}$	Transient tangle (I)(a)	2.1895	94.28
$3.272 \cdot 10^{-6}$	Chaotic tangle (I)(c)	2.1974	3.23
$3.149 \cdot 10^{-6}$	Non-chaotic tangle (I)(b)	2.2010	2.49
$3.060 \cdot 10^{-6}$	Transient tangle (I)(a)	2.2000	94.23
$1.477 \cdot 10^{-6}$	Chaotic tangle (I)(c)	2.2153	3.35
$1.448 \cdot 10^{-6}$	Non-chaotic tangle (I)(b)	2.2182	2.42
$1.378 \cdot 10^{-6}$	Transient tangle (I)(a)	2.2206	–
$6.547 \cdot 10^{-7}$	Chaotic tangle (I)(c)	2.2560	–
$6.500 \cdot 10^{-7}$	Non-chaotic tangle (I)(b)	2.2277	–

**3. Simulation results**

In this section, the results of the numerical simulations for Eq. (3) regarding the behavior described in **(I)**–**(IV)** of Section 1 are presented. The numerical simulations are performed using the fourth-order Runge–Kutta integration routine with a fixed step size.

**3.1. Simulation procedure**

The starting point is finding a pair of  $(\lambda_0, \gamma_0)$  such that the unforced system of Eq. (2) admits a homoclinic orbit. Then, Eq. (3) is integrated for the solutions in the neighborhood of the unperturbed homoclinic orbit. The following steps outline the simulation approach taken in obtaining the numerical results of this section:

1. Arbitrarily pick a  $\lambda_0 > 0$ , and select an initial position  $(q_0, p_0)$ , say  $q_0 = 0.01, p_0 = 0$ , and integrate Eq. (2) to find the corresponding value of  $\gamma_0$  for Fig. 1(a). The desired accuracy on the corresponding  $\gamma_0$  value is achieved using a bi-sectional approach by observing the point where the solution switches from the positive  $q$ -side to the negative  $q$ -side. For our purposes, a 12-digit accuracy on  $\gamma_0$  is found to be sufficient.
2. Substitute the above-found parameter values into Eq. (3) along with a fixed value of  $T$ , the period of the forcing function.

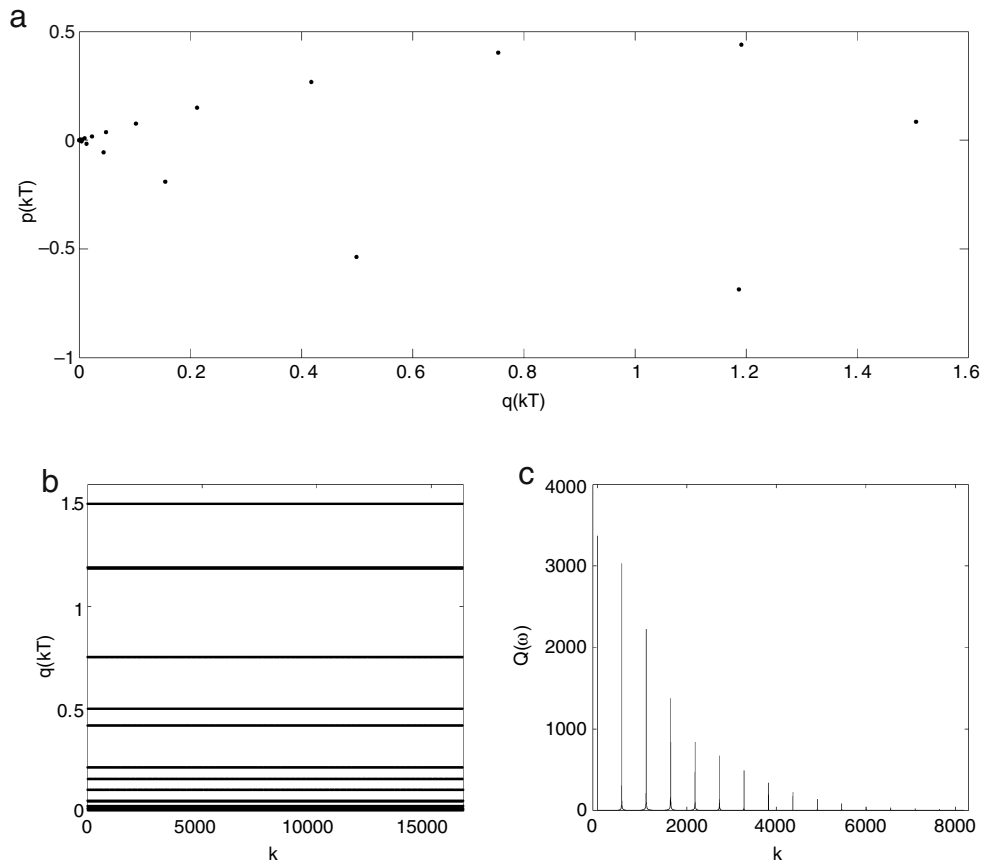


Fig. 2. An example of a sink for  $\mu = 7.2 \times 10^{-5}$ ,  $t_0 = 0.2$ , and  $T = 1$ .

Table 3  
Multiplicative periodicity on  $\mu$ .

$\lambda = 0.5$			
$\gamma = 0.577028548901$			
$T = 2.0$			
$\beta = 0.78077641$			
Theoretical multiplicity = $e^{\beta T} = 4.7662$			
$\mu$	Dynamical behavior	Actual ratio	Frequency of occurrence (%)
$1.239 \cdot 10^{-2}$	Transient tangle (I)(a)	–	93.30
$3.284 \cdot 10^{-3}$	Chaotic tangle (I)(c)	–	1.64
$3.124 \cdot 10^{-3}$	Non-chaotic tangle (I)(b)	–	5.06
$2.630 \cdot 10^{-3}$	Transient tangle (I)(a)	4.7110	93.39
$6.914 \cdot 10^{-4}$	Chaotic tangle (I)(c)	4.7498	1.60
$6.582 \cdot 10^{-4}$	Non-chaotic tangle (I)(b)	4.7463	5.01
$5.543 \cdot 10^{-4}$	Transient tangle (I)(a)	4.7447	94.47
$1.453 \cdot 10^{-4}$	Chaotic tangle (I)(c)	4.7584	0.69
$1.378 \cdot 10^{-4}$	Non-chaotic tangle (I)(b)	4.7765	4.83
$1.165 \cdot 10^{-4}$	Transient tangle (I)(a)	4.7579	93.42
$3.049 \cdot 10^{-5}$	Chaotic tangle (I)(c)	4.7655	1.71
$2.892 \cdot 10^{-5}$	Non-chaotic tangle (I)(b)	4.7649	4.87
$2.446 \cdot 10^{-5}$	Transient tangle (I)(a)	4.7629	93.45
$6.399 \cdot 10^{-6}$	Chaotic tangle (I)(c)	4.7648	1.71
$6.072 \cdot 10^{-6}$	Non-chaotic tangle (I)(b)	4.7628	4.85
$5.133 \cdot 10^{-6}$	Transient tangle (I)(a)	4.7652	–
$1.342 \cdot 10^{-6}$	Chaotic tangle (I)(c)	4.7683	–
$1.272 \cdot 10^{-6}$	Non-chaotic tangle (I)(b)	4.7736	–

3. Vary  $\mu$  and the initial time  $t_0$ , and for each fixed combination of  $\mu$  and  $t_0$ , integrate Eq. (3) to compute the corresponding solution. According to the theory of [11], the structure of the ho-

moclinic tangle is best revealed by the solutions for different initial times  $t_0$ . With  $(q_0, p_0)$  fixed throughout, the initial time  $t_0$  is run over the interval  $[0, T)$ , and the simulation results are compared to the predictions given in Section 1.

It is important to note that using a different initial phase position  $(q_0, p_0)$  does not change the qualitative nature of the simulation results, provided that it is inside of, and reasonably close to the homoclinic loop of Fig. 1(a). For the cases of (III) and (IV), we adjust the parameter  $\gamma$  to keep the stable and unstable manifolds of  $X^*$  separated.

The results presented in this section are obtained for the parameter values given in Table 1. Note that, for each of the  $(\lambda_0, \gamma_0)$  pair given in Table 1, Eq. (2) has a homoclinic loop.

### 3.2. Simulation results on (I)

In this subsection, we present sample plots for the dynamical objects listed in (I) of Section 1. As mentioned before, all parameters except  $\mu$  and  $t_0$  are fixed. The simulations of this subsection are conducted for a single set of parameter values from Table 1, namely  $(\lambda_0, \gamma_0, T) = (0.5, 0.577028548901, 1.0)$ . With these selected values, Eq. (3) is numerically integrated to produce a data set for the solution  $(q_{\mu, t_0}(t), p_{\mu, t_0}(t))$  satisfying  $(q_{\mu, t_0}(t_0), p_{\mu, t_0}(t_0)) = (q_0, p_0)$ . Sufficient transient time is allowed for the solutions to be pushed onto the homoclinic tangles. Then, the data points for one discrete orbit of the time- $T$  map are used to plot the following:

- (a)  $(q_{\mu, t_0}(kT), p_{\mu, t_0}(kT))$  on the  $(q, p)$ -plane for  $k \in \mathbb{N}^+$ .
- (b)  $(k, q_{\mu, t_0}(kT))$  (the redundancy of plotting  $(k, p_{\mu, t_0}(kT))$  is omitted here).
- (c) The Fourier spectrum of  $q_{\mu, t_0}(kT)$ .

**Table 4**  
Multiplicative periodicity on  $\mu$ .

$\lambda = 1.0$			
$\gamma = 1.122987493358$			
$T = 1.0$			
$\beta = 0.61803399$			
Theoretical multiplicity = $e^{\beta T} = 1.8552$			
$\mu$	Dynamical behavior	Actual ratio	Frequency of occurrence (%)
$1.470 \cdot 10^{-3}$	Transient tangle (I)(a)	–	94.75
$8.456 \cdot 10^{-4}$	Chaotic tangle (I)(c)	–	2.56
$8.287 \cdot 10^{-4}$	Non-chaotic tangle (I)(b)	–	2.69
$8.110 \cdot 10^{-4}$	Transient tangle (I)(a)	1.8126	94.87
$4.617 \cdot 10^{-4}$	Chaotic tangle (I)(c)	1.8315	1.96
$4.545 \cdot 10^{-4}$	Non-chaotic tangle (I)(b)	1.8233	3.18
$4.428 \cdot 10^{-4}$	Transient tangle (I)(a)	1.8315	94.96
$2.506 \cdot 10^{-4}$	Chaotic tangle (I)(c)	1.8424	2.37
$2.458 \cdot 10^{-4}$	Non-chaotic tangle (I)(b)	1.8491	2.67
$2.404 \cdot 10^{-4}$	Transient tangle (I)(a)	1.8419	94.93
$1.356 \cdot 10^{-4}$	Chaotic tangle (I)(c)	1.8481	2.45
$1.329 \cdot 10^{-4}$	Non-chaotic tangle (I)(b)	1.8495	2.63
$1.300 \cdot 10^{-4}$	Transient tangle (I)(a)	1.8492	94.96
$7.326 \cdot 10^{-5}$	Chaotic tangle (I)(c)	1.8509	1.87
$7.214 \cdot 10^{-5}$	Non-chaotic tangle (I)(b)	1.8423	3.16
$7.025 \cdot 10^{-5}$	Transient tangle (I)(a)	1.8505	95.026
$3.952 \cdot 10^{-5}$	Chaotic tangle (I)(c)	1.8537	2.78
$3.862 \cdot 10^{-5}$	Non-chaotic tangle (I)(b)	1.8679	2.20
$3.791 \cdot 10^{-5}$	Transient tangle (I)(a)	1.8531	95.02
$2.130 \cdot 10^{-5}$	Chaotic tangle (I)(c)	1.8554	4.35
$2.054 \cdot 10^{-5}$	Non-chaotic tangle (I)(b)	1.8802	0.63
$2.043 \cdot 10^{-5}$	Transient tangle (I)(a)	1.8556	94.92
$1.147 \cdot 10^{-5}$	Chaotic tangle (I)(c)	1.8570	3.07
$1.118 \cdot 10^{-5}$	Non-chaotic tangle (I)(b)	1.8372	2.01
$1.099 \cdot 10^{-5}$	Transient tangle (I)(a)	1.8590	94.98
$6.169 \cdot 10^{-6}$	Chaotic tangle (I)(c)	1.8593	4.46
$5.942 \cdot 10^{-6}$	Non-chaotic tangle (I)(b)	1.8814	0.56
$5.914 \cdot 10^{-6}$	Transient tangle (I)(a)	1.8583	–
$3.311 \cdot 10^{-6}$	Chaotic tangle (I)(c)	1.8632	–
$3.221 \cdot 10^{-6}$	Non-chaotic tangle (I)(b)	1.8449	–

All simulation results fall into one of the three types below:  
**(I)(a) Transient tangles.** One such instance occurs for  $\mu = 7 \cdot 10^{-7}$ . When  $t_0$  is run over  $[0, 1)$  with  $\Delta t_0 = 0.001$ , simulations show that all solutions pass the homoclinic tangle rather quickly to reach the negative  $q$ -side. Here, we have a transient tangle that contains no physical measures.

**(I)(b) Non-chaotic tangles.** Solutions for some  $t_0 \in [0, 1)$  stay on the positive  $q$ -side for all  $t$  and they all catch periodic sinks. One such instance is obtained for  $\mu = 5.92 \cdot 10^{-6}$ ,  $t_0 = 0.1$  as illustrated in Fig. 2.

**(I)(c) Chaotic tangles.** There are again cases of  $t_0 \in [0, 1)$  such that the solutions stay on the positive  $q$ -side for all  $t$ . However, the dynamical objects caught in this case are the Hénon-like attractors associated with transversal homoclinic tangency. An instance of this case is illustrated in Fig. 3 for  $\mu = 3.95 \cdot 10^{-5}$ ,  $t_0 = 0.1$ .

3.3. Simulations results on (II)

In this subsection we illustrate that the three dynamical scenarios, **(I)(a)–(c)**, of Section 1 repeat themselves in a fixed pattern that is periodic in  $\ln \mu^{-1}$  as  $\mu \rightarrow 0$ . The theoretical prediction of the period in  $\ln \mu^{-1}$  from [11] is  $\beta T$  where  $T$  is the period of the applied forcing and  $\beta$  is the unstable eigenvalue. Hence, the multiplicative period for a given  $\mu$ -cycle  $[\mu_k, \mu_{k+1}]$  is found to be

$$P = \mu_{k+1}/\mu_k \approx e^{\beta T}. \tag{4}$$

**Table 5**  
Multiplicative periodicity on  $\mu$ .

$\lambda = 1.0$			
$\gamma = 1.122987493358$			
$T = 2.0$			
$\beta = 0.61803399$			
Theoretical multiplicity = $e^{\beta T} = 3.4418$			
$\mu$	Dynamical behavior	Actual ratio	Frequency of occurrence (%)
$2.794 \cdot 10^{-2}$	Transient tangle (I)(a)	–	93.44
$9.428 \cdot 10^{-3}$	Chaotic tangle (I)(c)	–	2.09
$9.014 \cdot 10^{-3}$	Non-chaotic tangle (I)(b)	–	4.47
$8.128 \cdot 10^{-3}$	Transient tangle (I)(a)	3.4375	92.01
$2.728 \cdot 10^{-3}$	Chaotic tangle (I)(c)	3.4560	1.79
$2.623 \cdot 10^{-3}$	Non-chaotic tangle (I)(b)	3.4365	6.20
$2.259 \cdot 10^{-3}$	Transient tangle (I)(a)	3.5981	92.98
$7.958 \cdot 10^{-4}$	Chaotic tangle (I)(c)	3.4280	2.22
$7.609 \cdot 10^{-4}$	Non-chaotic tangle (I)(b)	3.4472	4.80
$6.854 \cdot 10^{-4}$	Transient tangle (I)(a)	3.2959	93.40
$2.312 \cdot 10^{-4}$	Chaotic tangle (I)(c)	3.4420	2.04
$2.213 \cdot 10^{-4}$	Non-chaotic tangle (I)(b)	3.4383	4.57
$1.991 \cdot 10^{-4}$	Transient tangle (I)(a)	3.4425	93.39
$6.719 \cdot 10^{-5}$	Chaotic tangle (I)(c)	3.4410	2.12
$6.419 \cdot 10^{-5}$	Non-chaotic tangle (I)(b)	3.4476	4.49
$5.785 \cdot 10^{-5}$	Transient tangle (I)(a)	3.4417	93.40
$1.951 \cdot 10^{-5}$	Chaotic tangle (I)(c)	3.4439	2.12
$1.864 \cdot 10^{-5}$	Non-chaotic tangle (I)(b)	3.4437	4.48
$1.680 \cdot 10^{-5}$	Transient tangle (I)(a)	3.4435	–
$5.669 \cdot 10^{-6}$	Chaotic tangle (I)(c)	3.4415	–
$5.418 \cdot 10^{-6}$	Non-chaotic tangle (I)(b)	3.4404	–

**Table 6**  
Summary of results on **(III)** and **(IV)**.

$(\lambda_0, \gamma_0) = (1.0, 1.122987493358)$		
$T = 1.0$		
$(q_0, p_0) = (0.01, 0.0)$		
$\mu = 2.733 \cdot 10^{-3}$		
Range of $\rho$	Dynamical behavior	Intersection of $W^s$ & $W^u$
$(1, 8.5) \times 10^{-6}$	Transient tangle (I)(a)	$W^s \cap W^u \neq \emptyset$
$(8.6, 9) \times 10^{-6}$	Non-chaotic sink (I)(c)	$W^s \cap W^u \neq \emptyset$
$(9.1, 9.7) \times 10^{-6}$	Non-chaotic sink	$W^s \cap W^u = \emptyset$
$(9.8, 10) \times 10^{-6}$	Hénon-like	$W^s \cap W^u = \emptyset$
$(1.1, 2.2) \times 10^{-5}$	Rank 1	$W^s \cap W^u = \emptyset$
$2.3 \times 10^{-5}$	Hénon-like	$W^s \cap W^u = \emptyset$
$(2.4, 2.5) \times 10^{-5}$	Rank 1 (weak)	$W^s \cap W^u = \emptyset$
$2.6 \times 10^{-5}$	Non-chaotic sink	$W^s \cap W^u = \emptyset$
$(2.7, 2.9) \times 10^{-5}$	Hénon-like	$W^s \cap W^u = \emptyset$
$(3, 14) \times 10^{-5}$	Non-chaotic sink	$W^s \cap W^u = \emptyset$
$(1.4, 1.5) \times 10^{-4}$	Transition to quasi-periodicity	$W^s \cap W^u = \emptyset$
$(> 1.5) \times 10^{-4}$	Quasi-periodicity	$W^s \cap W^u = \emptyset$

To illustrate this multiplicative periodicity of  $\mu$ , the simulation results of this subsection are presented in a tabular fashion. Tables 2 and 3 are obtained for  $(\lambda_0, \gamma_0) = (0.5, 0.577028548901)$  with  $T = 1, 2$ , respectively. Tables 4 and 5 are obtained for  $(\lambda_0, \gamma_0) = (1.0, 1.122987493358)$  and  $T = 1, 2$ , respectively.

To obtain these tabulated values, we proceed as follows:

- (a) For a given  $(\lambda_0, \gamma_0)$  pair, determine the value of the positive eigenvalue using

$$\beta = -\frac{\lambda_0}{2} + \sqrt{1 + \left(\frac{\lambda_0}{2}\right)^2} \tag{5}$$

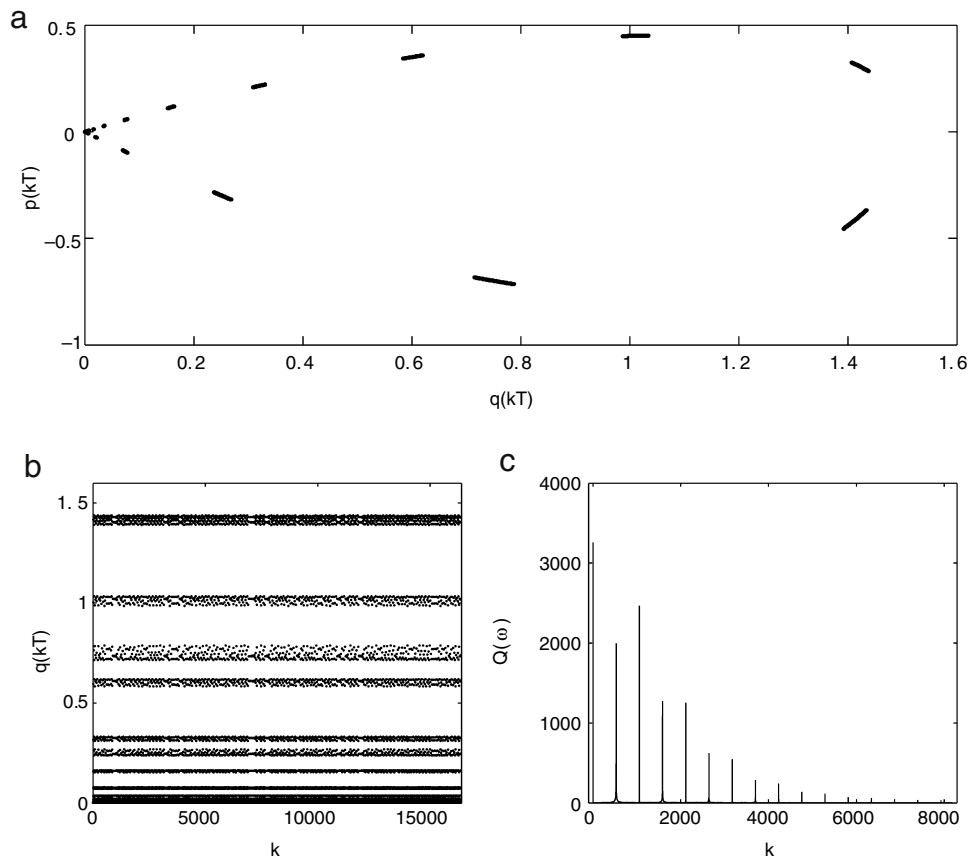


Fig. 3. An example of a chaotic tangle for  $\mu = 6.2 \times 10^{-6}$ ,  $t_0 = 1.7$ , and  $T = 1$ .

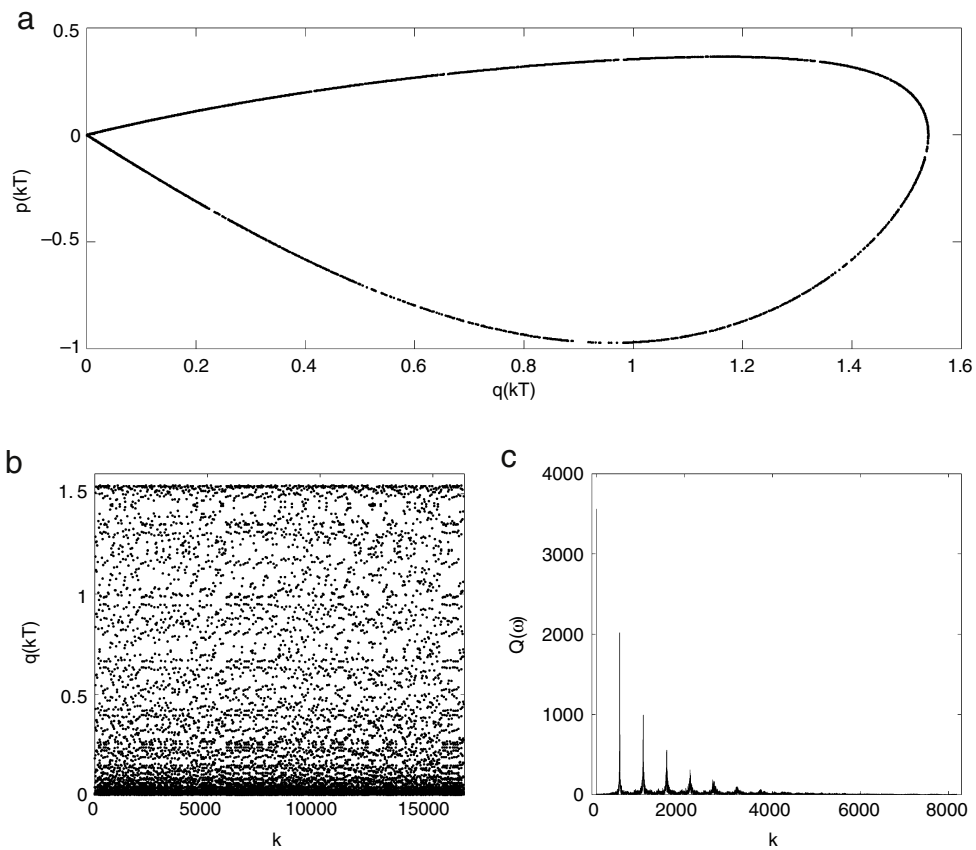


Fig. 4. A rank 1 attractor for  $\mu = 2.733 \times 10^{-3}$ ,  $\rho = 1.5 \times 10^{-5}$ .

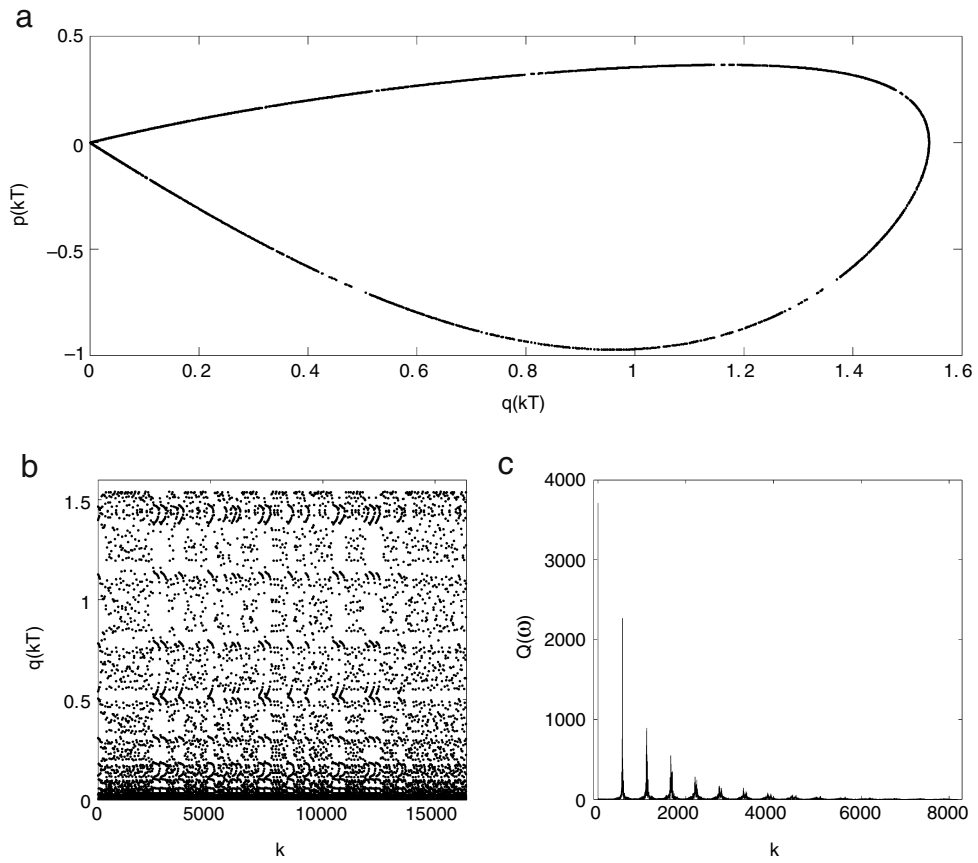


Fig. 5. A weak rank 1 attractor for  $\mu = 2.733 \times 10^{-3}$ ,  $\rho = 2.5 \times 10^{-5}$ .

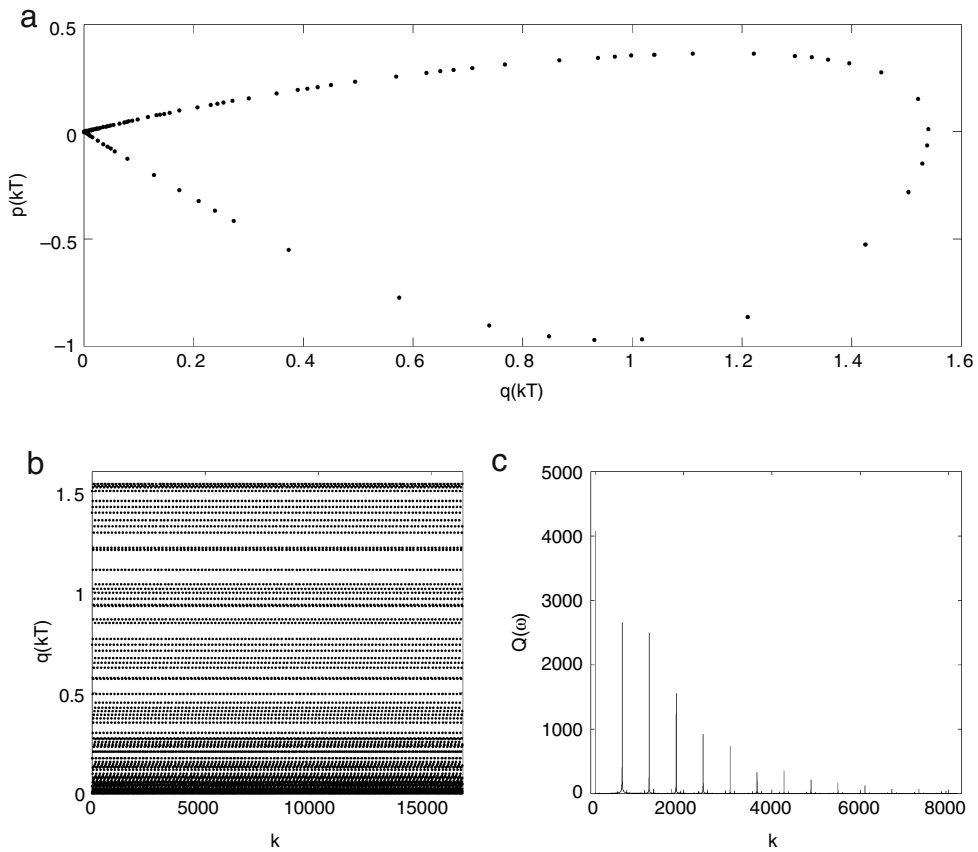


Fig. 6. Transition to quasi-periodic attractors,  $\mu = 2.733 \times 10^{-3}$ ,  $\rho = 1.4 \times 10^{-4}$ .

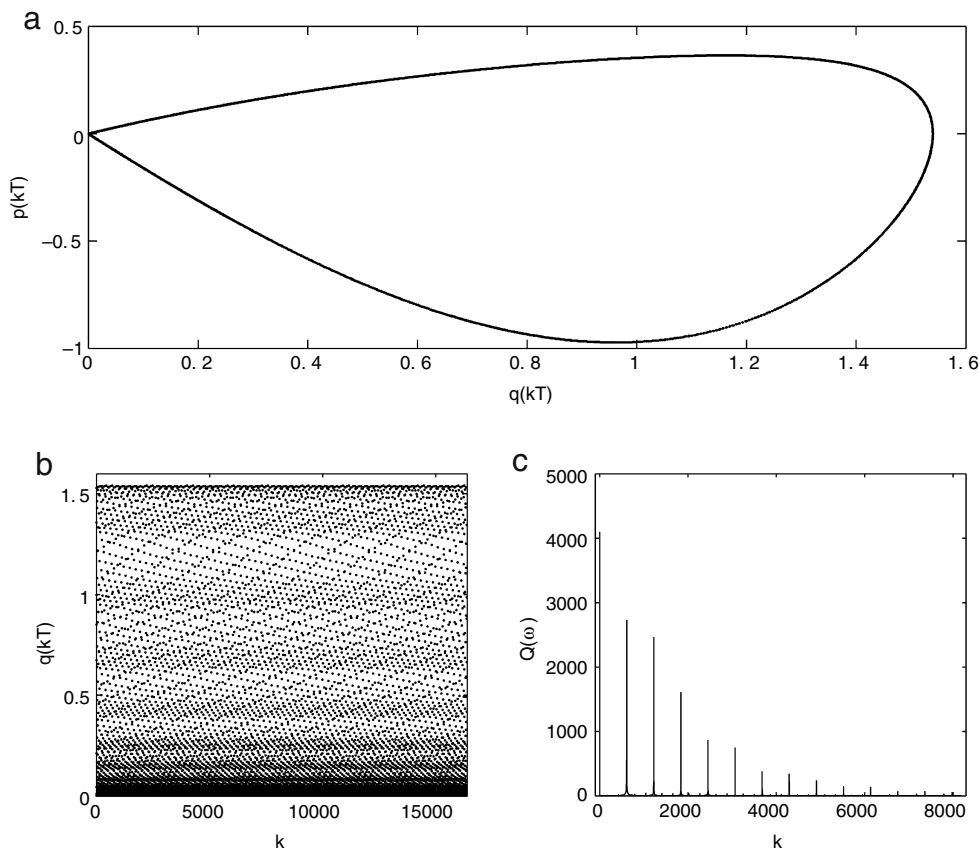


Fig. 7. A deformed quasi-periodic attractor for  $\mu = 2.733 \times 10^{-3}$ ,  $\rho = 1.5 \times 10^{-4}$ .

and compute, for a given  $T$ , the multiplicative ratio

$$P \approx e^{\beta T}.$$

Note that since the periodicity is for the 1D singular limit of the return map  $\mathcal{R}$  in [11], a slight deviation from  $P$  is expected for the corresponding ratio obtained from numerical simulations.

- (b) Fix the initial conditions at  $(q_0, p_0) = (0.01, 0.0)$ , and arbitrarily pick a  $\mu_0 \in [10^{-3}, 10^{-6}]$ . The end-of-cycle  $\mu$  value is approximated by letting  $\mu_1 \approx P\mu_0$ .
- (c) Then, integrate Eq. (3) for a fixed  $\mu \in [\mu_0, \mu_1]$  by varying  $t_0$  over  $t_0 \in [0, T)$  with  $\Delta t_0 = 0.001$  to determine the type of the observed dynamical object. All simulation results fall into one of the following three types:
  - (i) All computed solutions reach the negative  $q$ -side. Here, a *transient tangle* is recorded.
  - (ii) There is at least one  $t_0 \in [0, T)$  for which the solution remains on the positive  $q$ -side for all  $t$ , and the plots of all such solutions look like that of Fig. 2. Here, a *non-chaotic tangle* is recorded.
  - (iii) There is at least one  $t_0 \in [0, T)$  for which the solution remains on the positive  $q$ -side for all  $t$ , and the plots of such solutions look like that of Fig. 3. In this case, a *chaotic tangle* (a Hénon-like attractor) is recorded.
- (d) Then, this process is repeated to cover other  $\mu$ -intervals. In Tables 2–5, only the transitional  $\mu$ -values where the dynamics changes from one type to another are listed in the  $\mu$ -column. For example, in Table 2, for all  $\mu \in [7.6 \cdot 10^{-4}, 7.28 \cdot 10^{-4})$ , we have *non-chaotic tangles*, and for all  $\mu \in [7.28 \cdot 10^{-4}, 3.57 \cdot 10^{-4})$ , we have *transient tangles*.

The values in the *actual ratio* column are computed by taking the inverse of the ratio of the  $\mu$  value for one behavior type within the current cycle to the  $\mu$  value for the same behavior type of the previous cycle. The last column, *frequency of occurrence*, is computed

by taking the ratio of the  $\mu$ -range for a given behavior type to the whole  $\mu$ -range for the same cycle. It indicates the relative measure of the set of  $\mu$ -values for each behavior type within a  $\mu$ -cycle. In other words, if a given row has 94.2% for the behavior type *transient tangle*, then the simulations will result in a *transient tangle* for 94.2% of the  $\mu$  values within that cycle.

**Remark.** As shown in Tables 2–5, the values of  $\mu$  for transient tangles occur much more frequently (>90% of the time) than the other two cases combined. Thus, with a random pick of a  $\mu$  value, it is much more likely to hit a transient tangle. The theoretical estimate of the multiplicative ratio is used as a guide in our search for the other two types. It works quite well most of the time, and in a few unexpected cases, a slightly adjusted  $\mu$  value always works. It can also be observed from these tables that the multiplicative ratios obtained from simulations are all reasonably close to the value predicted by the theory.

### 3.4. Simulation results on (III) and (IV)

In this subsection, we present the simulation results for (III) and (IV) of Section 1. First, we rewrite the parameter  $\gamma$  in Eq. (3) as

$$\gamma = \gamma_0 - \mu\rho \tag{6}$$

where  $\gamma_0$  is the corresponding parameter value for  $\lambda_0$  as given in Table 1,  $\mu$  is the magnitude of forcing as before.  $\rho$  is a new parameter used to control the value of  $\gamma$ . Let  $W^u$  and  $W^s$  be the stable and the unstable manifolds of the perturbed periodic solution from  $q(t) = 0$ . In order for (III) and (IV) of Section 1 to appear it is required that  $W^u \cap W^s = \emptyset$ .  $\rho$  is the parameter used to adjust the distance between  $W^s$  and  $W^u$ .

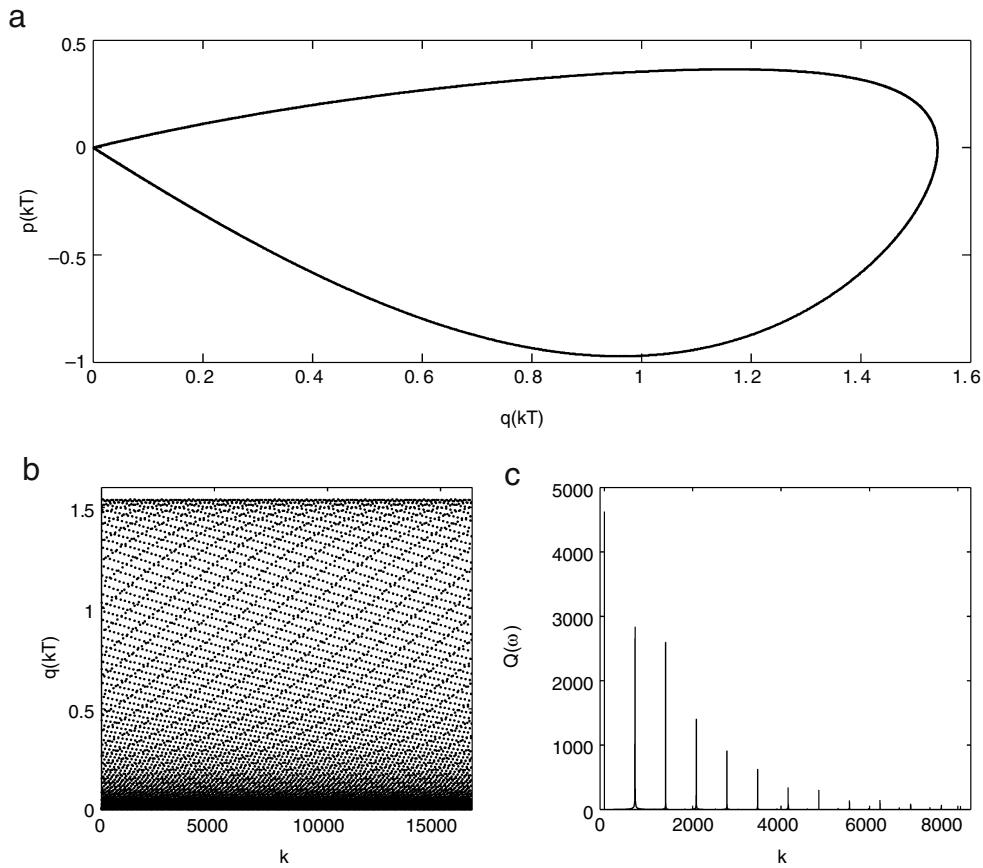


Fig. 8. A quasi-periodic attractor for  $\mu = 2.733 \times 10^{-3}$ ,  $\rho = 1 \times 10^{-3}$ .

The numerical simulations of this section are conducted for a single  $\mu$  value with

$$\begin{aligned}
 (\lambda_0, \gamma_0) &= (1.0, 1.122987493358) \\
 T &= 1.0 \\
 (q_0, p_0) &= (0.01, 0.0) \\
 \mu &= 0.002733.
 \end{aligned}
 \tag{7}$$

With the parameter values given in Eq. (7), Eq. (3) is integrated for different values of  $\rho$  and different initial times  $t_0 \in [0, T)$ . By varying  $\rho$ , the distance between  $W^s$  and  $W^u$  is adjusted, and the orbits integrated demonstrate the behavior specified in (III) and (IV) of Section 1. As before, we will present the result of individual simulations by plotting (a) one orbit for the time- $T$  map in the  $(q, p)$ -space, (b) the time evolution of the  $q$ -component of the same orbit, and (c) the frequency spectrum for the  $q$ -component.

We verify, numerically, that there exists a  $\rho_t > 0$  such that for  $0 \leq \rho < \rho_t$ ,  $W^s$  and  $W^u$  intersect transversally. For these  $\rho$  values, we are still in the case of homoclinic tangles, and thus, the observed dynamical phenomena are still those of (I)(a)–(c). This implies that there are values of  $t_0 \in [0, T)$  for which the solutions starting from  $(q_0, p_0)$  at  $t_0$  pass through the homoclinic tangle to reach the negative  $q$ -side. For  $\rho > \rho_t$ ,  $W^s$  and  $W^u$  are pulled apart. For  $\rho$  larger than but close to  $\rho_t$ , the behavior of the system of Eq. (3) can be that of a non-chaotic attractor admitting sinks, or that of a Hénon-like attractor, or that of a rank 1 attractor with SRB measures and full stochastic behavior. In any case, for all  $\rho > \rho_t$ , no solution starting from  $(q_0, p_0)$  at any given initial time  $t_0$  will ever reach the negative  $q$ -side. As  $\rho$  gets larger, the expansions in the time direction gradually diminish, causing all solutions to be attracted to a two-dimensional torus.

The simulation results for this subsection are as follows: At  $\rho = 0$ , we have a chaotic tangle with a Hénon-like attractor of Fig. 3. Further simulations show that between  $\rho = 1.0 \cdot 10^{-6}$  and  $8.5 \cdot 10^{-6}$ , we have transient tangles. Between  $\rho = 8.6 \cdot 10^{-6}$  and  $9 \cdot 10^{-6}$ , we have non-chaotic tangles with sinks. The value of  $\rho_t$  appears to be in between  $9 \cdot 10^{-6}$  and  $9.1 \cdot 10^{-6}$ . For  $\rho = 9 \cdot 10^{-6}$ , when  $t_0$  is varied over  $[0, T)$  with an increment of  $\Delta t_0 = 0.01$ , only four solutions (for  $t_0 = 0.03, 0.33, 0.74, 0.87$ ) out of a total of one hundred reach the negative  $q$ -side, whereas for  $\rho = 9.1 \cdot 10^{-6}$ , out of a total of one thousand solutions obtained by setting  $\Delta t_0 = 0.001$ , none reaches the negative  $q$ -side.

From  $\rho = 9.1 \cdot 10^{-6}$  to  $9.7 \cdot 10^{-6}$ , we obtain non-chaotic attractors dominated by sinks. It must be emphasized that, for  $\rho \geq 9.1 \cdot 10^{-6}$ ,  $W^s$  and  $W^u$  are completely separated, and all solutions stay on the positive  $q$ -side forever. The plots of individual orbits are qualitatively the same as that of Fig. 2. However, we note that here we have a dynamical scenario completely different from the non-chaotic tangles of (I)(b) of Section 1. For the non-chaotic tangles of (I)(b), solutions for more than half of the  $t_0 \in [0, T]$  values reach the negative  $q$ -side. But, in the current case, all solutions will stay on the positive  $q$ -side to catch a sink.

As  $\rho$  is increased further, to values between  $\rho = 9.8 \cdot 10^{-6}$  and  $1 \cdot 10^{-5}$ , we hit Hénon-like attractors similar to that of Fig. 3. We again caution that the current case is different from the corresponding case of (I)(c), because, now, the solutions for all  $t_0 \in [0, T]$  remain on the positive  $q$ -side reflecting the fact that  $W^u \cap W^s = \emptyset$ .

For  $\rho$  values between  $1.1 \cdot 10^{-5}$  and  $2.2 \cdot 10^{-5}$ , we encounter rank 1 attractors. One such instance is shown in Fig. 4. The differences between Figs. 3 and 4 are striking. Unlike Fig. 3, Fig. 4 is no longer dominated by one periodic orbit, a fact that is also reflected in the continuous spectrum of Fig. 4(c).

At  $\rho = 2.3 \cdot 10^{-5}$  we again have a Hénon-like attractor. For  $\rho \in (2.4, 2.5) \times 10^{-5}$ , we have what we call a weak rank 1 attractor. An orbit for  $\rho = 2.5 \cdot 10^{-5}$  is plotted in Fig. 5. This appears to be a transitional case, where an SRB measure and a weak sink coexist.

We have a case of non-chaotic sinks for  $\rho = 2.6 \cdot 10^{-5}$ . In between  $\rho = 2.7 \cdot 10^{-5}$  and  $2.9 \cdot 10^{-5}$ , we again hit Hénon-like attractors, and for  $\rho$  values between  $3 \cdot 10^{-5}$  and  $1.3 \cdot 10^{-4}$ , we have non-chaotic attractors with sinks. As  $\rho$  is further increased, a transition to quasi-periodic attractors occurs. Such a transitional case for  $\rho = 1.4 \cdot 10^{-4}$  is shown in Fig. 6. Another case for  $\rho = 1.5 \cdot 10^{-4}$  is shown in Fig. 7, where the quasi-periodic behavior is still seriously deformed. For  $\rho > 1.5 \cdot 10^{-4}$ , quasi-periodic attractors appear to settle in. Such a case for  $\rho = 1 \cdot 10^{-3}$  is shown in Fig. 8 where the quasi-periodic behavior is more pronounced.

A brief summary outlining the qualitatively different behaviors that the system of Eq. (3) demonstrates with varying  $\rho$  is given in Table 6.

**Remark.** The difference between  $\rho_t$  and the value of  $\rho$  where the quasi-periodic attractors first appear is  $\sim 10^{-4}$ . Consequently, the corresponding measure for the parameter  $\gamma$  is  $\approx \mu \times 10^{-4} \sim 10^{-6}$ . Note that this measure would be even smaller for smaller  $\mu$  values. Therefore, it is not likely that one will observe the attractors illustrated in Figs. 4–6 through random searches without the theoretical guidance of [10].

#### 4. Conclusions

In this paper, we have systematically studied, through numerical simulations, the complicated dynamics of periodically perturbed homoclinic solutions for a dissipative saddle. The majority of the dynamical phenomena discussed in this paper are new, and they are observed in numerical simulations under the guidance of a recent theory developed in [10,11].

Our simulations illustrated that, when the stable and the unstable manifolds of a dissipative saddle intersect transversally, the dynamical objects are of three main types. The first type is the *transient tangles*. These tangles contain no physical measures. The second type is the *non-chaotic tangles*. For tangles of this type, periodic sinks are the dominating dynamical object. The third type is the *chaotic tangles*. They admit Sinai–Ruelle–Bowen measures associated with Hénon-like attractors. These strange attractors are related to the tangential intersections of the stable and the unstable manifolds of the saddles from Smale's horseshoe. We remark that Smale's horseshoe exists in the dynamical behaviors of all three types mentioned above. Horseshoes, however, are not associated with any physical measure.

Our simulations also verified that, as  $\mu \rightarrow 0$ , the homoclinic tangles of the three types emerge *periodically*, repeating in an accelerated fashion with a multiplicative period that was analytically predicted in [11]. The actual multiplicative period computed from the simulation data matches the predicted value given by the theory of [11].

When the stable and the unstable manifolds of the dissipative saddle are pulled apart, our simulations confirmed that, before quasi-periodic attractors set in, there is a narrow window of parameters where we observe attractors of three types: namely, the non-chaotic type dominated by periodic sinks; the Hénon-like type; and the rank 1 attractors. Quasi-periodic attractors emerge as the stable and the unstable manifolds of the dissipative saddle are pulled further apart.

Through the theory of [10,11], we now know comprehensively what to expect in numerical simulations of periodically perturbed homoclinic solutions. It is also worth noting that the values of the magnitude of forcing employed in illustrating the above behaviors are between  $10^{-3}$  and  $10^{-7}$ , much smaller than the values commonly used in numerical studies.

#### References

- [1] H. Poincaré, Les Méthodes Nouvelles de la Mécanique Céleste, vol. 3, Gauthier-Villars, Paris, 1892.
- [2] G.D. Birkhoff, Nouvelles recherches sur les systèmes dynamiques, Mem. Pont. Acad. Sci. Novi Lyncaei 1 (1935) 85–216.
- [3] S. Smale, Differentiable dynamical systems, Bull. Amer. Math. Soc. 73 (1967) 474–817.
- [4] V.K. Melnikov, On the stability of the center for time periodic perturbations, Trans. Moscow Math. Soc. 12 (1963) 1–57.
- [5] J. Guckenheimer, P. Holmes, Nonlinear oscillations, dynamical systems and bifurcation of vector fields, in: Appl. Math. Sci., vol. 42, Springer-Verlag, Berlin, 1983.
- [6] J.K. Moser, Stable and Random Motions in Dynamical Systems (with Special Emphasis on Celestial Mechanics), Princeton University Press, Princeton, NJ, 1973.
- [7] J. Palis, F. Takens, Hyperbolicity & sensitive chaotic dynamics at homoclinic bifurcations, in: Cambridge Studies in Advanced Mathematics, vol. 35, Cambridge University Press, Cambridge, 1993.
- [8] L.P. Shilnikov, A.L. Shilnikov, D.V. Turaev, L.O. Chua, Methods of qualitative theory in nonlinear dynamics. Part I, in: World Scientific Series on Nonlinear Science, Series A: Monographs and Treatises, vol. 4, World Scientific Publishing Co., River Edge, NJ, 1998.
- [9] L.P. Shilnikov, A.L. Shilnikov, D.V. Turaev, L.O. Chua, Methods of qualitative theory in nonlinear dynamics. Part II, in: World Scientific Series on Nonlinear Science, Series A: Monographs and Treatises, vol. 5, World Scientific Publishing Co., River Edge, NJ, 2001.
- [10] Q. Wang, W. Ott, Dissipative homoclinic loops and rank one chaos, 2007 (preprint).
- [11] Q. Wang, A. Oksasoglu, Dynamics of homoclinic tangles in periodically perturbed second-order equations, 2007 (preprint).
- [12] Y.G. Sinai, Gibbs measure in ergodic theory, Russian Math. Surveys 27 (1972) 21–69.
- [13] D. Ruelle, A measure associated with axiom A attractors, Amer. J. Math. 98 (1976) 619–654.
- [14] R. Bowen, Equilibrium states and the ergodic theory of Anosov diffeomorphisms, in: Lecture Notes in Math., Springer, Berlin, 1976.
- [15] Q. Wang, L.-S. Young, Strange attractors with one direction of instability, Comm. Math. Phys. 218 (2001) 1–97.
- [16] Q. Wang, L.-S. Young, Toward a theory of rank one attractors, Ann. Math. 167 (2008) 349–480.
- [17] Q. Wang, L.-S. Young, From invariant curves to strange attractors, Commun. Math. Phys. 225 (2002) 275–304.
- [18] M. Hénon, A two-dimensional mapping with a strange attractor, Comm. Math. Phys. 50 (1976) 69–77.
- [19] Q. Wang, A. Oksasoglu, Rank one chaos: Theory and applications, Internat. J. Bifur. Chaos. 18 (2008) 1–59.
- [20] L.-S. Young, What are SRB measures, and which dynamical systems have them? J. Stat. Phys. 108 (2002) 733–754.